Information-rich localization microscopy through machine learning

Taehwan Kim[1†], Seonah Moon[2†], & Ke Xu[2,3]

[1]*Department of Electrical Engineering and Computer Sciences, University of California, Berkeley, CA 94720*

[2]*Department of Chemistry, University of California, Berkeley, CA 94720*

[3]*Chan Zuckerberg Biohub, San Francisco, CA 94158*

[†]*These authors contributed equally*

While current single-molecule localization microscopy (SMLM) methods often rely on the target-specific alteration of the point spread function (PSF) to encode the multidimensional contents of single fluorophores, we argue that the details of the PSF in an unmodified microscope already carry rich, multidimensional information. We introduce a data-driven method in which artificial neural networks (ANNs) are trained to make a direct link between an experimental PSF image and its underlying parameters. To demonstrate this concept in real systems, we deciphered in fixed cells both the colors and the axial positions of single-molecule emitters from regular SMLM data.

Originally developed toward the specific goal of superior spatial resolution, single-molecule localization (super-resolution) microscopy (SMLM), including STORM/(F)PALM[1–3] and PAINT[4], has emerged in recent years as a generic tool for sampling diverse biologically relevant information at the nanoscale[5]. For example, when combined with environment-sensitive dyes, intracellular heterogeneity in local chemical environment can be mapped by concurrently obtaining the spatial positions and emission spectra of millions of single fluorescent molecules[6]. Consequently, the full potential of SMLM is expected to be unleashed through the proper multidimensional analysis of the emission wavelength[5], brightness, dipole orientation[7], as well as the axial (3D) position[8] of single molecules.

To date, to extract information beyond the in-plane location, e.g., the emission wavelength and the axial location, of single emitters, would often oblige the explicit encoding of such high-dimensionality information into the diffraction pattern of single molecules (point spread functions; PSFs) through optical aberrations and alterations[5,8], including astigmatism[9], interference[10], wavelength-dependent splitting[11], dispersion[12], and wave-front modification[13]. The resultant, engineered PSF shape and intensity then help establish direct relationships between experimental observables and fluorophore characteristics. Such approaches, each often optimized for a single parameter of interest, inevitably increase the PSF size and/or necessitate the splitting of fluorescence across different channels, and so often incur complicated optics and compromised performances between different parameters. While recent work[14,15] has studied the PSF design for the simultaneous estimation of color and axial position, added optics and enlarged PSFs are still involved, and proper calibration of such Fourier optics-heavy systems is challenging[16].

We reason that even the simplest PSF obtained from an unmodified microscope is rich in information—in addition to the axial location embedded in the defocused PSF, which has been examined in recent work[17,18], the emission wavelength of a fluorophore also sets the scale of PSF in all three dimensions[19]. Contributions from the two sources are distinct yet subtle, and would be hard to decouple via simple models given the difficulties in fully characterizing all system-specific properties.

We present a data-driven approach in which the relationship between a PSF image, obtained from an unmodified commercial microscope, and the underlying multidimensional characteristics of an emitter is directly established by a supervised machine learning algorithm. A related approach has been recently used in astronomy for stellar classification[20]. Although SMLM faces additional challenges associated with the vast range of axial positions (as opposed to stars always at infinity), it benefits from the ready access to arbitrary amounts of experimental PSFs that may be acquired under identical conditions. By training generic learning models using such datasets, an end-to-end framework from raw PSF images to the molecule characteristics can be constructed.

To demonstrate this concept, we developed a method for machine learning-based 3D multi-color SMLM (**Fig. 1** and **Methods**). With typical experimental pixel sizes (~100 nm), the dimensionality of the PSF images is moderate (modeled as 13×13 pixels), and thus artificial neural networks (ANN) with multiple hidden layers[21] were directly used as our learning model. ANN is beneficial here as it possesses excellent representational power; moreover, since ANN does not require domain-specific expertise to construct nonlinear models, it offers a facile means to train different target parameters in an end-to-end fashion.

65 One ANN with a final Softmax layer was first trained using cross-entropy loss to
66 determine the emitter color of each presented PSF. Once trained, the final Softmax output
67 provided an estimate for the conditional probability distribution of the fluorophore color, which
68 enabled the classification of each PSF image with known confidence (**Fig. 1a** and **Methods)**. For
69 this color-separating ANN, training data for different fluorophores were separately prepared
70 from multiple imaging sessions performed under the same experimental conditions as the final
71 sample, but using only one known fluorophore at a time. The training data contained sufficient
72 samples for fluorophores at different axial positions within the depth of field (~±500 nm of the
73 focal plane), so that the ANN was trained to recognize fluorophores for all axial positions.

74 In parallel, ANNs for resolving the axial position of the emitter were separately trained
75 for each fluorophore using L2 loss so that the final output was a scalar value[22] corresponding to
76 the decoded axial position (**Fig. 1b**). Training data for these axial-localization ANNs were
77 collected by step-scanning samples each containing one specific fluorophore, as is typically
78 performed for the calibration in existing 3D SMLM methods[9].

79 Once both trainings were completed, SMLM data from unknown samples were localized
80 in 2D, and the single-molecule images were first fed into the above color-separating ANN (**Fig.**
81 **1c**). The resultant, color-separated single-molecule images were then separated fed into the
82 above axial-localization ANNs trained with the corresponding fluorophores (**Fig. 1c**).
83 Multidimensional SMLM data were thus obtained by combining the ANN results with the initial
84 2D-localization results.

85 We first examined the performance of the color-separating ANN using two types of 40-
86 nm fluorescent beads that differed by 45 nm in emission wavelength ("yellow" and "orange").

87 When the beads are at the focal plane, fitting to simple Gaussian models yielded PSF sizes (2σ)
88 that were directly proportional to the emission wavelength (**Fig. 2a**), as expected. At photon
89 counts of 3000-4000, this difference gave adequate separation of the two colors (**Fig. 2a**).
90 However, this separation quickly fell apart when results from different axial positions are mixed:
91 unsurprisingly, defocusing led to substantially increased PSF sizes, and so this parameter no
92 longer offers useable color separation (**Fig. 2b**).

93 In contrast, our color-separating ANN recognized the nuances in the PSF patterns due to
94 differences in color vs. differences in axial position, and thus offered excellent color separation
95 both in the presence and absence of defocusing (**Fig. 2cd**). As mentioned, the output of this ANN
96 represents the conditional probabilities of each given image being classified as certain types of
97 fluorophores. In the binary yellow-orange system, the results can be simplified as the difference
98 Δ between the two probabilities of being orange and being yellow for every image (**Fig. 2cd**).
99 Even in the presence of defocusing, simple classification based on $\Delta>0$ and $\Delta<0$ already gave
100 ~90% accuracy at 1000-1500 photons, and accuracies of >96% are reached at >3,000 photons
101 (**Fig. 2e**), a value readily achieved in STORM imaging. The results can be further improved by
102 only keeping classifications with $|\Delta|$ above a given confidence threshold, at the expense of
103 rejecting classifications of lower confidences. For example, adopting a confidence threshold of
104 0.8 helps improve the identification accuracy at 1000-1500 photons to 96%, with a rejection rate
105 of 21% (**Fig. 2e**). Our ANN approach is thus tunable for different applications.

106 We next applied our approach to cell imaging (**Fig. 3**). The microtubules and
107 mitochondria in adherent COS-7 cells were respectively immunolabeled with two STORM dyes,
108 CF568 and Alexa Fluor 647 (AF647). Both dyes were excited within the same STORM imaging
109 session, and resultant single-molecule fluorescence was collected after a multi-notch filter. For

110 training of the first, color-separating ANN, COS-7 cells singly-labeled by CF568 and AF647 for
111 microtubules were STORM-imaged on the same setup, which naturally contained single
112 molecules at different axial positions within the depth of field. For training of the second, axial-
113 localization ANN, dye-labeled antibodies were attached to the coverslip for step-scanning in the
114 axial direction (**Methods**).

115 **Figure 3a** presents the acquired STORM image colored by the fitted Gaussian width (2σ)
116 of the PSF of each molecule. Whereas it is clear that all the narrowest widths belonged to
117 microtubules, which were stained by the shorter-wavelength dye CF568, larger widths were
118 found at both microtubules and mitochondria (e.g., cyan arrows in **Fig. 3a**). This result is similar
119 to what we found in the bead data (**Fig. 2b**): defocusing broadens the PSF width, and so this
120 simple parameter can no longer be used to separate colors. Remarkably, our color-separating
121 ANN achieved excellent color separation for the entire image independent of axial position (and
122 thus defocusing) (**Fig. 3b-d**), and consistent results were obtained on different cells over
123 repeated experiments (**Supplementary Fig. 1**). Quantification of the color separation (**Fig. 3f**)
124 indicated that at a confidence threshold of 0.8 (~20% rejection rate), a ~88.4% accuracy is
125 achieved for molecules emitting 3000 photons, and the accuracy quickly increased to 98.5% for
126 ~5000 photons, a value often achieved in STORM.

127 Based on this successful color classification, two axial-localization ANNs, each trained
128 for AF647 and CF568, were next used to separately decode the axial positions of the molecules
129 in the two color channels, the results of which were recombined into one image for presentation
130 (**Fig. 3e** and **Supplementary Fig. 1**). This showed the expected result that the cell edges, thinner
131 in height, were dominated by small z values, whereas for regions far away for the cell edges, the
132 cells became thicker and had increased z values. White arrows in **Fig. 3ae** further point to

133 regions of microtubules, labeled by the same CF568 dye, where similarly increased PSF widths
134 were noted, but the ANN correctly identified one being below the focal plane whereas the other
135 above. We further note that as the two color channels are successfully separated, they may also
136 be separated fed into other recent methods that extract axial positions from unmodified PSFs[17,18].

137 Our finding highlights the rich, multidimensional information concealed in the details of
138 the diffraction-limited image of a fluorophore, which was uniquely unleashed in this work
139 through state-of-the-art machine learning algorithms. We note that our approach is not limited to
140 a particular type of PSF or machine-learning algorithm. The co-evolution of our data-driven
141 analysis scheme with the ongoing efforts on PSF engineering[8] should thus lead to new
142 improvements, and conceivably, fundamentally new types of imaging modalities, for
143 multidimensional SMLM.

Figures

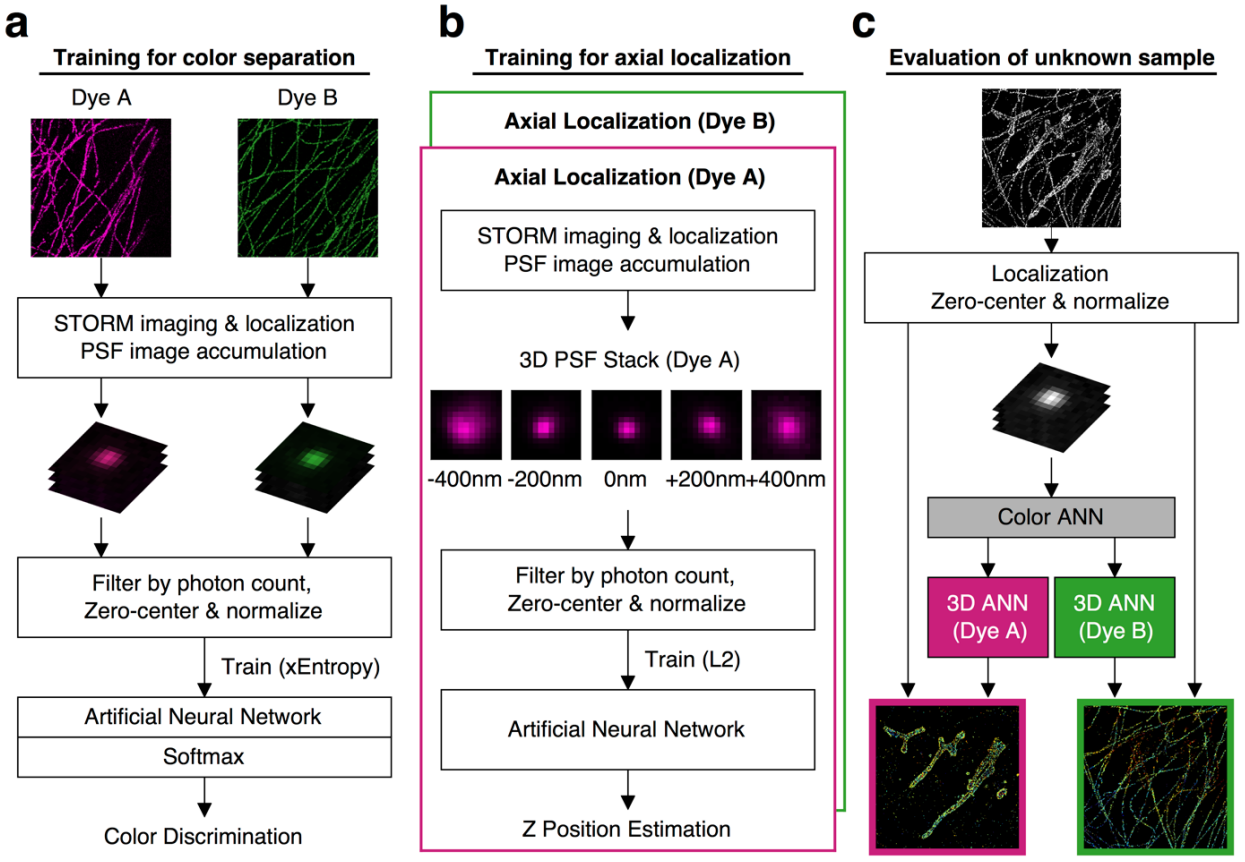

Fig. 1 | Workflow of the machine learning-based multidimensional SMLM. (a) A color-separating ANN is trained using samples each singly labeled by one known fluorophore, in which PSFs at different axial positions are well-represented. **(b)** ANNs for resolving the axial position are separately trained for each fluorophore using PSFs of known axial positions. **(c)** For the analysis of unknown samples, single-molecule images are localized in 2D, and first fed into the color-separating ANN described in (**a**). The color-separated single-molecule images are then separately fed into the axial-localization ANNs trained with the corresponding fluorophores, as described in (**b**). The resultant color and axial position information is then combined with the 2D localization of each molecule to generate the final multidimensional SMLM data.

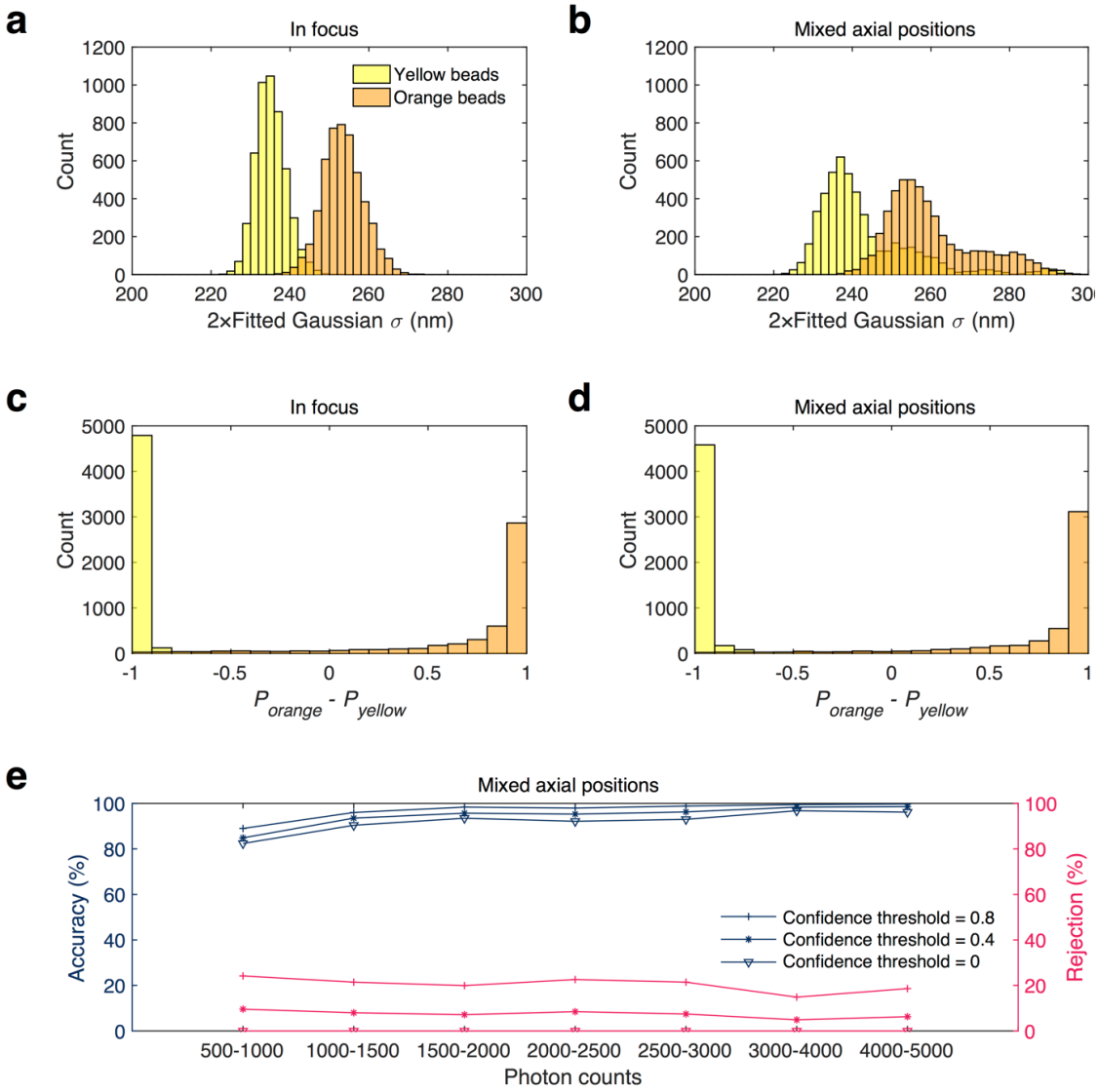

Fig. 2 | Performance of the color-separating ANN for fluorescent beads. (**a-b**) PSF size (2σ of 2D Gaussian fitting) distribution of "yellow" and "orange" beads emitting 3000-4000 photons, for (**a**) all beads are right at the focal plane and (**b**) the focus is evenly scanned over ±200 nm of the focal center. (**c-d**) Outputs of our color-separating ANN on the same datasets, presented as the distribution for the differences in the evaluated probabilities of each bead being "orange" vs. being "yellow". (**e**) Accuracy of classification (left axis) and rejection rate (right axis) in the presence of defocusing as a function of photon count, for confidence thresholds of 0, 0.4, and 0.8.

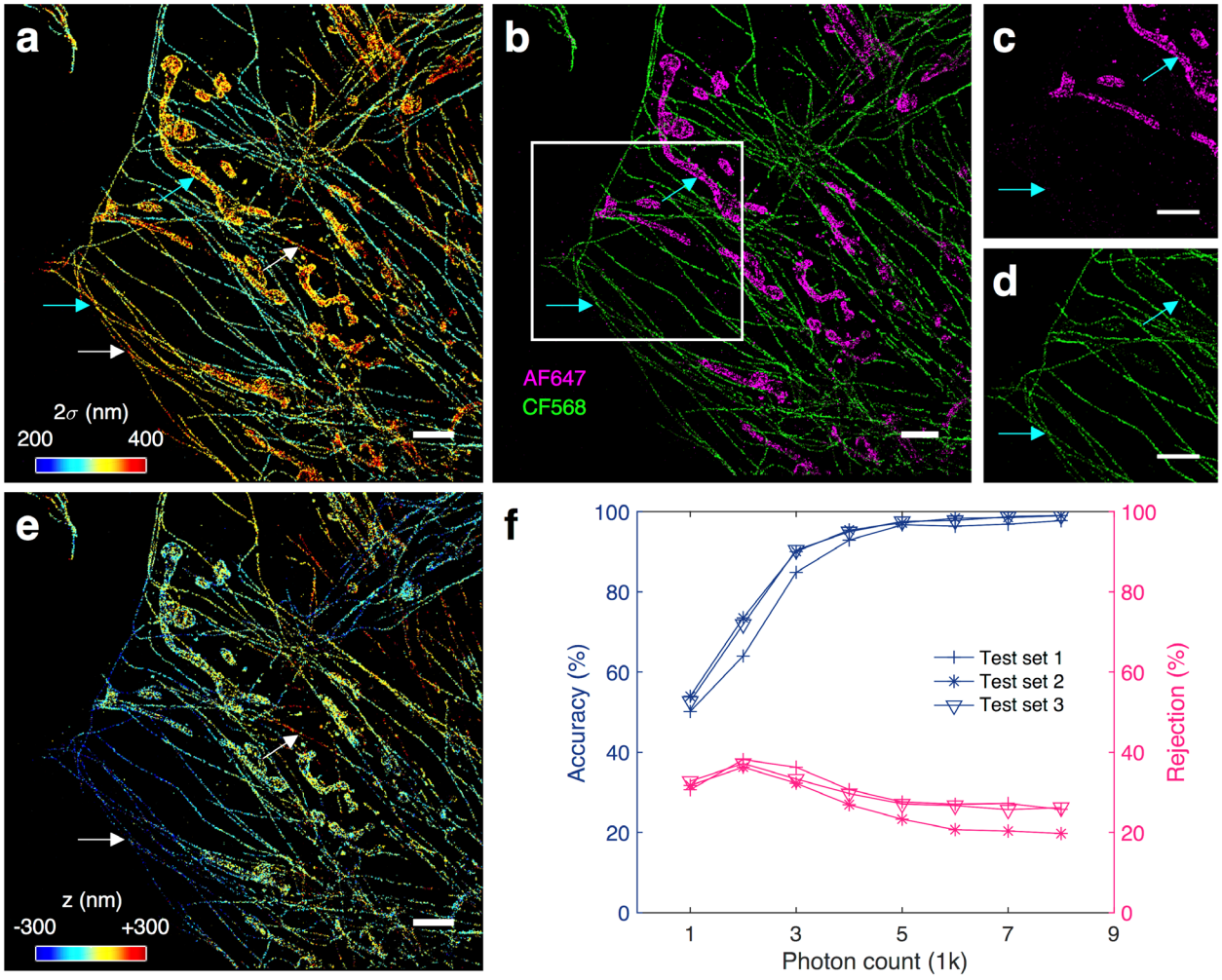

Fig. 3 | ANN-resolved multicolor 3D SMLM in cells based on unmodified PSFs. (**a**) STORM image of CF568-labeled microtubules and AF647-labeled mitochondria in a fixed COS-7 cell, colored by the fitted Gaussian width (2σ) of the PSF of each molecule. **(b)** Result of the color-separating ANN at a confidence threshold of 0.8. (**c-d**) The separated AF647 (**c**) and CF568 (**d**) channels for the boxed area in (**b**). **(e)** The merged 3D STORM image after separately determining the axial position of every single molecule based on the ANNs respectively trained for AF647 and CF568. Color here presents the axial position (*z*), with blue being closest to the substrate and red being the farthest away. Cyan arrows in (**a-d**) point to regions where molecules of similar PSF widths are correctly determined as different colors by the ANN. White arrows in (**a**) and (**e**) point to regions of the same CF568 labeling that showed similar defocusing effects, but determined by ANN as being on opposite sides of the focal plane. Scale bars, 2 μm (**a-e**). **(f)** Classification accuracy (left axis) and rejection rate (right axis) of the color-separating ANN as a function of photon count across different data sets, at a confidence threshold of 0.8.

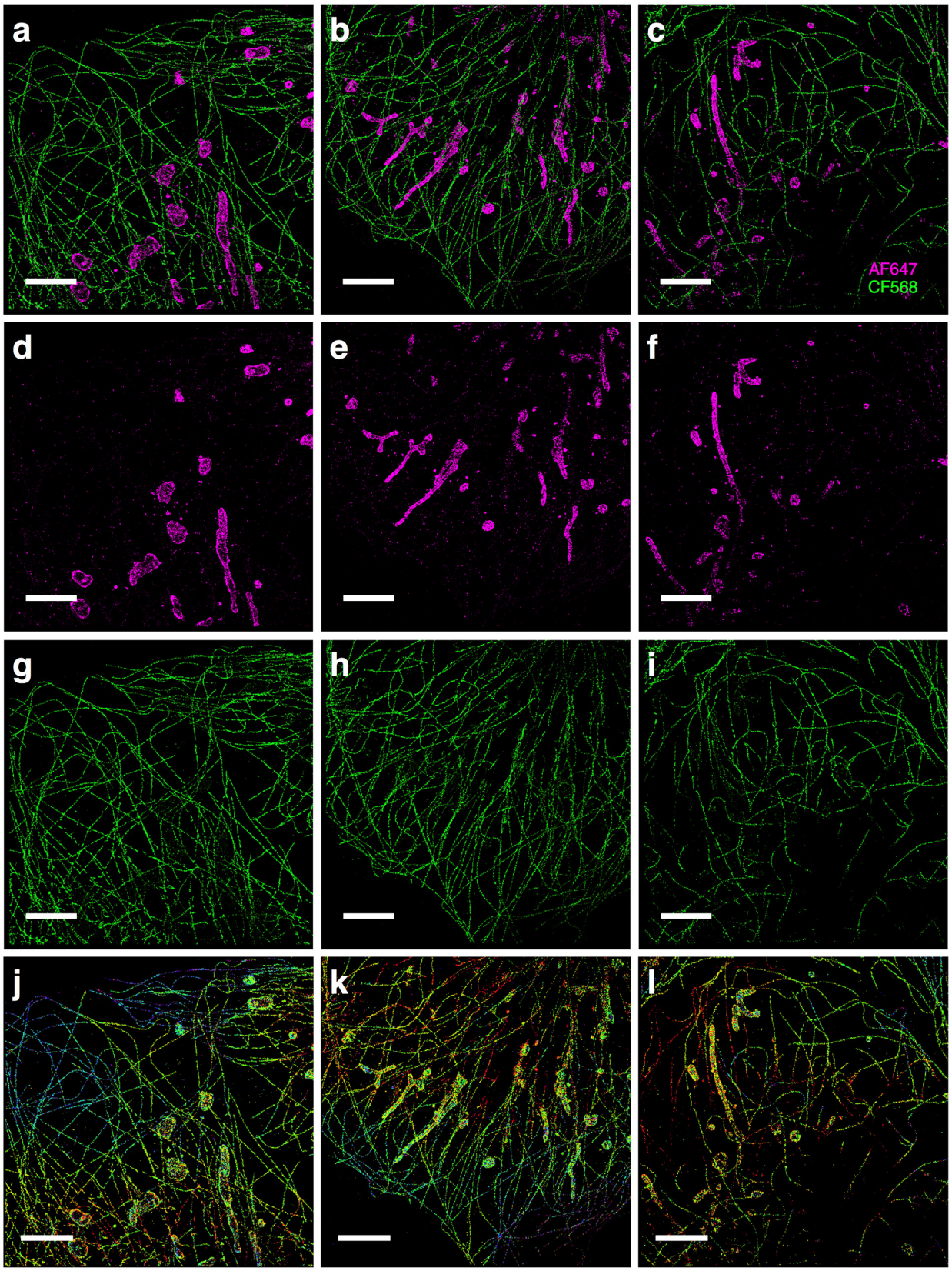

Supplementary Fig. 1. Additional examples of ANN-resolved multicolor 3D SMLM in cells based on unmodified PSFs. Scale bars, 4 μm.

Methods

Optical setup. STORM and bead experiments were performed on a Nikon Ti-E inverted fluorescence microscope using an oil-immersion objective lens (Nikon CFI Plan Apochromat λ 100×, NA 1.45) and the native 1.5x magnification on the microscope, without any modifications to the imaging path. Lasers emitting at 644, 561, and 488 nm were introduced to the back focal plane of the objective lens via a multi-line dichroic mirror (ZT405/488/561/640rpc-uf2, Chroma). A translation stage shifted the laser beams toward the edge of the objective lens so that they entered slightly below the critical angle, illuminating ~1 μm into the sample. Emission was filtered by a multi-notch filter (ZET405/488/561/640m, Chroma) and recorded by an EM-CCD camera (iXon Ultra 897, Andor). Effective magnification and pixel size were ~150x and ~107 nm, respectively.

Bead samples. 40 nm dia. fluorescent beads from Invitrogen (F10720; "yellow" and "orange" FluoSpheres with emission peaks at 515 and 560 nm, respectively) were diluted in Dulbecco's phosphate buffered saline (DPBS), sealed between a glass slide and a pre-cleaned #1.5 thickness coverslip, and imaged with the above optical setup. The 488-nm and 561-nm lasers were used to excite the two types of beads to similar levels of brightness. To record images at different axial positions, the objective lens was scanned by the built-in motor over a range of −200 to +200 nm of the focal plane.

Cell samples. COS-7 cells were plated on #1.5 coverslips to achieve a confluency of ~50% in ~1.5 days, and fixed with 0.1% glutaraldehyde and 3% paraformaldehyde in DPBS at room temperature. The sample was quenched with 0.1% sodium borohydride in DPBS and rinsed with DBPS three times. Primary and secondary antibodies were diluted in a blocking buffer (3% BSA + 0.1% Triton X-100 in DPBS) and labeled as described previously[9]. Primary antibodies were

204 mouse anti-tubulin (Abcam ab7291) for microtubules and rabbit anti-Tom20 (Santa Cruz sc-
205 11415) for mitochondria. Secondary antibodies were AF647-labeled goat anti-mouse IgG1
206 (Invitrogen A21240) and donkey anti-rabbit secondary conjugated with a CF568 succinimidyl
207 ester (Biotium 92131). The sample was mounted in a STORM buffer [10% (w/v) glucose, 120
208 mM cysteamine, 0.8 mg/mL glucose oxidase, and 40 μg/mL catalase in Tris-HCl (pH 7.5)] and
209 imaged using the optical setup described above. The sample was illuminated with the 644 and
210 561nm lasers at ~2 kW/cm^2, which led to the photoswitching of AF647 and CF568 single
211 molecules. Fluorescence was recorded by the EM-CCD for a frame size of 256x256 pixels at 55
212 frames per second. Each movie was typically recorded for 20,000 frames.

213 **Antibody samples.** Training data for the axial localization of AF647 and CF568 single
214 molecules were acquired using the above AF647- and CF568-labeled secondary antibodies. The
215 two antibodies were separately diluted in DPBS to ~2 μg/mL. Pre-cleaned #1.5 coverslips were
216 separately incubated in either solution for ~5 min, briefly air-dried, rinsed with distilled water,
217 and mounted and imaged as described above. To record single-molecule images at different axial
218 positions, the objective lens was scanned by the built-in motor in the range of −700 to +700 nm
219 of the focal plane.

220 **Preprocessing of single-molecule images for ANNs.** Single-molecule fluorescence in raw
221 STORM and bead data was first identified and localized in 2D using established methods[1].
222 Single-molecule PSF images were cropped as 13x13 pixels surrounding the 2D localizations; at
223 this time, images containing multiple emitting molecules were rejected. The cropped PSF images
224 were zero-centered, and their L2/Euclidean norm was normalized before being used as inputs for
225 ANNs.

Design and implementation of neural networks. An ANN architecture comprising multiple hidden layers was implemented using the Tensorflow framework on a computer with 32GB RAM, Intel i7-7800X CPU, and Nvidia GTX-1080Ti GPU. The same architecture was used for both the color-separating and axial-localization ANNs (4 total layers of 4096-4096-2048-1024 neurons, respectively). Each hidden layer was fully connected, and rectified linear units were used as their activation function. For color discrimination, Softmax function and cross-entropy were used for loss calculation, the weights in the network were not directly included for regularization, and a dropout layer was inserted before the final layer to prevent over-fitting. For axial localization, the output of the final layer was set to be a scalar value, and L2 norm was used to calculate the learning loss for each batch. In this case, L2 norm of the weights in each layer was added to the loss function for regularization, and dropout was not used. Network hyper-parameters such as the number of neurons in each layer (given above), the dropout ratio (0.5 for the color-separating ANN), and the regularization factor (0.01 for the axial-localization ANNs) were adjusted for optimized performance.

Neural network training. Since the network is subject to handling input images with various noise levels, it was important to maintain a consistent noise level within the training dataset regardless of the classification class or axial location. Therefore, experimental PSF images with comparable photon counts of 4500-5500 were used throughout the training process, and molecules with photon counts higher than this range were used for the validation during the training process to check the generalization of the trained network. The weights initialized by the Xavier method[23] are trained using the Adam optimization algorithm. An initial learning rate of 10^{-4} and 10^{-3}, and a batch size of 64 and 32 were used for the color-separating and the axial-localization ANNs, respectively. The learning rate was set to decrease by ~5x after every 1,000

iterations. The sizes of the training sets were ~10,000 and ~6,000 per fluorophore type for the color-separating and the axial-localization ANNs, respectively. The networks converged within ~10 epochs (training time: 231.9 s for the color-separating ANN, and 488.5 s for the axial-localization ANN).

Neural network inference. At the inference stage, input single-molecule PSF images were first plugged into the color-separating ANN. This ANN provides a conditional probability distribution corresponding to the input image. Specifically, when the size of each input image is N by N pixels, and there are M different molecule color classes, the final output from the Softmax layer for the ith input image is

$$P(y_i|x_i),\ x_i \in \mathbb{R}^{N\times N},\ y_i \in \{\text{Dye 1}, \cdots, \text{Dye M}\}. \tag{1}$$

From this distribution, the ANN makes the decision in a maximum-likelihood manner: the molecule color class with the highest probability is chosen. This, in turn, implies that we can use this distribution to quantify the classification confidence. For example, in a simple binary classification problem, the confidence for the color assignment of the ith input image can be evaluated as

$$|\Delta_i| = |P(\text{Dye 1}|x_i) - P(\text{Dye 2}|x_i)|. \tag{2}$$

By setting a finite confidence threshold δ to reject molecules with low classification confidences ($|\Delta_i|<\delta$), improved classification accuracy may be obtained (e.g., Fig. 2e). This parameter may thus be adjusted by the user to balance the classification accuracy and rejection rate. Once the color of the molecule is determined, the single-molecule image is plugged into the axial-localization ANN trained for that particular color to evaluate the axial position. With GPU acceleration, both inference steps (passing the forward path of the neural networks) were

extremely fast: only ~300 ms was used to infer 100,000 molecules for both the color-separating and the axial-localization ANNs.

Acknowledgments

This work was in part supported by the Beckman Young Investigator Program and the Packard Fellowships for Science and Engineering. K.X. is a Chan Zuckerberg Biohub investigator. T.K. acknowledges support from Kwanjeong Educational Foundation. S.M. acknowledges support from Samsung Scholarship.

References

1. Rust, M. J., Bates, M. & Zhuang, X. Sub-diffraction-limit imaging by stochastic optical reconstruction microscopy (STORM). *Nat. Methods* **3,** 793–796 (2006).
2. Betzig, E. *et al.* Imaging intracellular fluorescent proteins at nanometer resolution. *Science* **313,** 1642–1645 (2006).
3. Hess, S. T., Girirajan, T. P. K. & Mason, M. D. Ultra-high resolution imaging by fluorescence photoactivation localization microscopy. *Biophys. J.* **91,** 4258–4272 (2006).
4. Sharonov, A. & Hochstrasser, R. M. Wide-field subdiffraction imaging by accumulated binding of diffusing probes. *Proc. Natl. Acad. Sci.* **103,** 18911–18916 (2006).
5. Yan, R., Moon, S., Kenny, S. J. & Xu, K. Spectrally resolved and functional super-resolution microscopy via ultrahigh-throughput single-molecule spectroscopy. *Acc. Chem. Res.* **51,** 697–705 (2018).
6. Moon, S. *et al.* Spectrally resolved, functional super-resolution microscopy reveals nanoscale compositional heterogeneity in live-cell membranes. *J. Am. Chem. Soc.* **139,** 10944–10947 (2017).
7. Backlund, M. P., Lew, M. D., Backer, A. S., Sahl, S. J. & Moerner, W. E. The role of molecular dipole orientation in single-molecule fluorescence microscopy and implications for super-resolution imaging. *ChemPhysChem* **15,** 587–599 (2014).
8. von Diezmann, A., Shechtman, Y. & Moerner, W. E. Three-dimensional localization of single molecules for super-resolution imaging and single-particle tracking. *Chem. Rev.* **117,** 7244–7275 (2017).

9. Huang, B., Wang, W., Bates, M. & Zhuang, X. Three-dimensional super-resolution imaging by stochastic optical reconstruction microscopy. *Science* **319,** 810–813 (2008).

10. Shtengel, G. *et al.* Interferometric fluorescent super-resolution microscopy resolves 3D cellular ultrastructure. *Proc. Natl. Acad. Sci.* **106,** 3125–3130 (2009).

11. Bossi, M. *et al.* Multicolor far-field fluorescence nanoscopy through isolated detection of distinct molecular species. *Nano Lett.* **8,** 2463–2468 (2008).

12. Zhang, Z., Kenny, S. J., Hauser, M., Li, W. & Xu, K. Ultrahigh-throughput single-molecule spectroscopy and spectrally resolved super-resolution microscopy. *Nat. Methods* **12,** 935–938 (2015).

13. Pavani, S. R. P. *et al.* Three-dimensional, single-molecule fluorescence imaging beyond the diffraction limit by using a double-helix point spread function. *Proc. Natl. Acad. Sci.* **106,** 2995–2999 (2009).

14. Shechtman, Y., Weiss, L. E., Backer, A. S., Lee, M. Y. & Moerner, W. E. Multicolour localization microscopy by point-spread-function engineering. *Nat. Photonics* **10,** 590–594 (2016).

15. Smith, C., Huisman, M., Siemons, M., Grünwald, D. & Stallinga, S. Simultaneous measurement of emission color and 3D position of single molecules. *Opt. Express* **24,** 4996 (2016).

16. Siemons, M., Hulleman, C. N., Thorsen, R. Ø., Smith, C. S. & Stallinga, S. High precision wavefront control in point spread function engineering for single emitter localization. *Opt. Express* **26,** 8397–8416 (2018).

17. Franke, C., Sauer, M. & van de Linde, S. Photometry unlocks 3D information from 2D localization microscopy data. *Nat. Methods* **14,** 41–44 (2016).

18. Li, Y. *et al.* Real-time 3D single-molecule localization using experimental point spread functions. *Nat. Methods* **15,** 367–369 (2018).

19. Gibson, S. F. & Lanni, F. Diffraction by a circular aperture as a model for three-dimensional optical microscopy. *J. Opt. Soc. Am. A* **6,** 1357 (1989).

20. Kuntzer, T., Tewes, M. & Courbin, F. Stellar classification from single-band imaging using machine learning. *Astron. Astrophys.* **591,** A54 (2016).

21. Bishop, C. M. *Neural networks for pattern recognition*. (Oxford University Press, Inc., 1995).

22. Hara, K., Vemulapalli, R. & Chellappa, R. Designing deep convolutional neural networks for continuous object orientation estimation. *ArXiv170201499 Cs* (2017).

23. Glorot, X. & Bengio, Y. Understanding the difficulty of training deep feedforward neural networks. in *Proceedings of the Thirteenth International Conference on Artificial Intelligence and Statistics* 249–256 (2010).